Electron spectroscopy of rare-gas clusters irradiated by x-ray free-electron laser pulses from SACLA

H Fukuzawa[1,2], T Tachibana[1], K Motomura[1], W Q Xu[1]‡, K Nagaya[2,3], S Wada[2,4], P Johnsson[5], M Siano[6], S Mondal[1], Y Ito[1], M Kimura[1], T Sakai[3], K Matsunami[3], H Hayashita[4], J Kajikawa[4], X-J Liu[7]§, E Robert[7], C Miron[7,8], R Feifel[9,10], J P Marangos[6], K Tono[11], Y Inubushi[2], M Yabashi[2], M Yao[3], and K Ueda[1,2]

[1]Institute of Multidisciplinary Research for Advanced Materials, Tohoku University, Sendai 980-8577, Japan
[2]RIKEN SPring-8 Center, Kouto 1-1-1, Sayo, Hyogo 679-5148, Japan
[3]Department of Physics, Kyoto University, Kyoto 606-8502, Japan
[4]Department of Physical Science, Hiroshima University, Higashi-Hiroshima 739-8526, Japan
[5]Department of Physics, Lund University, P.O. Box 118, 22100 Lund, Sweden
[6]Blackett Laboratory, Imperial College London, London SW7 2AZ, United Kingdom
[7]Synchrotron SOLEIL, L'Orme des Merisiers, Saint-Aubin, BP 48, FR-91192 Gif-sur-Yvette Cedex, France
[8]Extreme Light Infrastructure - Nuclear Physics (ELI-NP), "Horia Hulubei" National Institute for Physics and Nuclear Engineering, 30 Reactorului Street, RO-077125 Măgurele, Jud. Ilfov, Romania
[9]Department of Physics and Astronomy, Uppsala University, P.O. Box 516, SE-751 20 Uppsala, Sweden
[10]Department of Physics, University of Gothenburg, SE-412 96 Gothenburg, Sweden
[11]Japan Synchrotron Radiation Research Institute (JASRI), Kouto 1-1-1, Sayo, Hyogo 679-5198, Japan

E-mail: `fukuzawa@tagen.tohoku.ac.jp` (H. Fukuzawa)

E-mail: `ueda@tagen.tohoku.ac.jp` (K. Ueda)

Abstract. We have measured electron energy spectra and asymmetry parameters of Ar clusters and Xe clusters illuminated by intense X-rays at 5 and 5.5 keV. A velocity map imaging spectrometer was developed for this purpose and employed at an x-ray free-electron laser facility, SACLA in Japan. The cluster size dependence and the peak fluence dependence of the electron spectra and asymmetry parameters are discussed.

‡ Present address: Department of Mathematics and Physics, Bengbu University, Bengbu 233030, Anhui, China
§ Present address: School of Physics and Nuclear Energy Engineering, BeiHang University, Beijing 100191, China

1. Introduction

In early 2012, an x-ray free-electron laser (XFEL) facility, the SPring-8 Angstrom Compact free electron LAser (SACLA) [1], started user operation in Japan. Currently, there are only two XFEL facilities that are in operation in the world; LCLS [2] in USA, which started user operation in late 2009, and SACLA. One of the most promising applications of XFELs may be to determine unknown structures of nano-sized objects and macromolecules by single-shot x-ray imaging [3, 4, 5, 6, 7]. Another related demonstrated application of XFEL is serial femtosecond x-ray diffraction (SFX) of protein (nano)crystals [8, 9, 10, 11, 12, 13, 14], which has been revealing structures of protein molecules that could not be determined by the conventional synchrotron-based x-ray diffraction. These measurements fully rely on the unique properties of XFEL radiation, such as the transverse coherence and extremely high brigthness of the ultrafast, intense x-ray pulse. Such novel approaches are revolutionizing the field of the structure determination. At the same time, they are entering a new regime of x-ray–matter interaction. This provokes an important interrogation regarding the electronic damage that may occur in femtosecond time scale [15, 16] during this interaction.

The new regime of x-ray–matter interaction above mentioned has opened new possibilities in the creation of matter in extreme conditions [17, 18, 19, 20, 21]. Irradiating solid density matter with the tightly focused XFEL pulse transfers a huge amount of energy into it in a very short time, resulting in creation of plasmas at solid densities and at high temperatures. Such matter is called warm dense matter at temperatures of a few electron volts, or hot dense matter at temperatures of tens to hundreds electron volts [22]. Study of matter in extreme conditions created by the XFEL pulse is indeed a rapidly growing area.

At SACLA, in order to study this new regime of x-ray–matter interaction and also to accumulate information about electron and nuclear dynamics that may cause radiation damage in the XFEL-based structure studies, we have been investigating reaction dynamics in atoms [23, 24], molecules [25] and clusters [26] irradiated by the intense XFEL pulses. To study gas-phase atomic and molecular reactions we have been using ion mass spectrometry [23, 24] and three-dimensional ion momentum spectroscopy [25]. To study cluster reactions, especially nanoplasma creation by the XFEL radiation to the solid-density atomic clusters, we have been using electron spectroscopy [26].

In the present paper, we report extensive experimental investigations of electron emission from Ar and Xe clusters irradiated by the intense hard x-ray ($\sim$5 keV) XFEL pulses from SACLA. A subset of the spectra were reported in Tachibana et al. [26] together with a full account of theoretical modeling. Electron emission from rare-gas clusters irradiated by FELs in the extreme ultraviolet (EUV) range have been extensively investigated previously both experimentally and theoretically [27, 28, 29, 30, 31, 32, 33, 34, 35]. It is known via these earlier studies that a nonoplasma is formed from rare gas clusters upon irradiation of EUVFEL pulses. In the case of EUVFEL pulses, the main heating mechanism is photoionization itself. Photoelectrons released from the

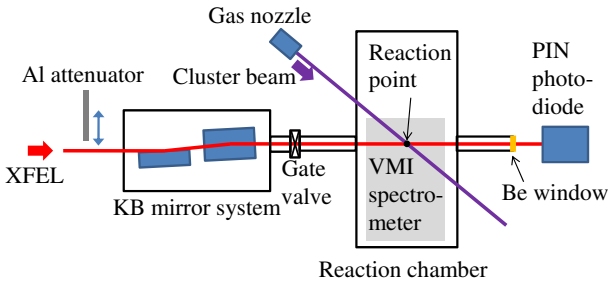

Figure 1. Schematic experimental arrangement.

individual atoms in the clusters are trapped by the highly charged cluster ion and form nanoplasma. When a rare-gas cluster is irradiated by the intense hard x-ray FEL pulse, on the other hand, nanoplasma is formed due to secondary electron emission instead of photoemission [26].

The present paper is organized in the following manner. The next section, section 2, describes our experimental setup, as well as the experimental procedures and the data analysis. Section 3 presents results and discussions, while section 4 concludes the present work.

2. Experiment

2.1. Configuration

The experimental configuration is depicted in figure 1. The experiment was carried out at the experimental hutch 3 (EH3) of beamline 3 (BL3) at SACLA in Japan [36, 37]. The photon energies were 5 keV and 5.5 keV. The photon band width was ∼60 eV (FWHM). The repetition rate of the XFEL pulses was 10 Hz. The pulse width was estimated to be 10 fs (FWHM) [37]. A Kirkpatrick-Baez (KB) mirror system with a focal length of ∼1.4 m is permanently installed at EH3 [38]. The XFEL beam was focused by the KB mirror system to a focal size of ∼1 μm (FWHM) in diameter with a Rayleigh length of ∼8 mm.

The rare-gas clusters were prepared by adiabatic expansion of the rare gas (Ar or Xe) through a 250 μm nozzle at room temperature [39]. The stagnation pressures were 0.43, 0.67 and 1.12 MPa for Ar and 0.14, 0.21, 0.32, 0.51, 0.86 and 1.50 MPa for Xe. The averaged cluster sizes $\langle N \rangle$ were estimated to be ∼80, ∼300 and ∼1000 for Ar and ∼80, ∼300, ∼1000, ∼3000, ∼10000 and ∼37000 for Xe, respectively, according to the well-known scaling law [40, 41, 42]. The uncertainty of $\langle N \rangle$ due to the fluctuation of the stagnation pressure was estimated to be ±20%. The cluster beam was skimmed by two skimmers placed at 20 and 400 mm from the nozzle. The inner diameters of the 1st and 2nd skimmers were 0.5 and 2 mm, respectively. The distance between the 2nd skimmer and the interaction point was 250 mm. The cluster beam at the interaction point was estimated to be ∼2 mm (FWHM) in diameter. Thus the source volume of the ions was

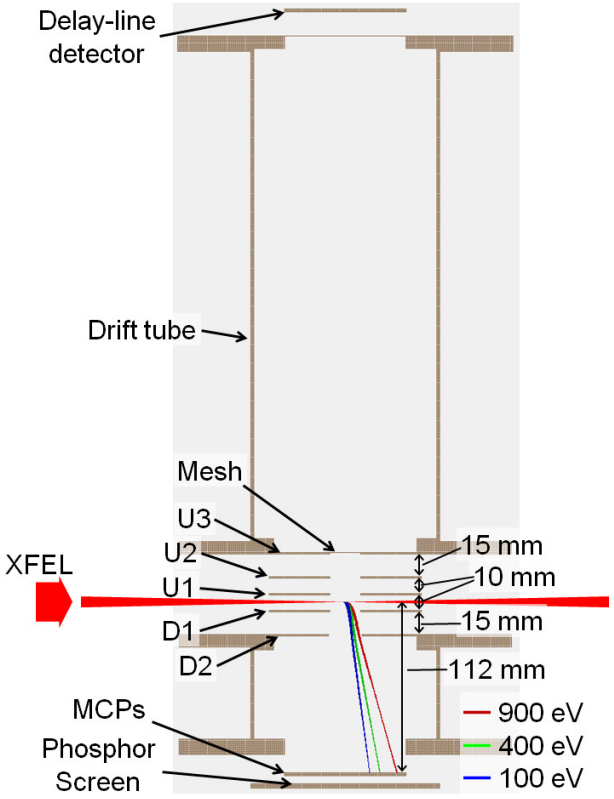

Figure 2. Configuration of the velocity map imaging spectrometer.Simulated trajectories of the electrons with kinetic energy of 100, 400 and 900 eV are shown. In the simulations, electron source points are distributed ±1 mm from the reaction point along the XFEL propagation direction and electron emission directions are of perpendicular to the spectrometer axis.

roughly of cylindrical shape of ∼1 μm in diameter and ∼2 mm along the XFEL beam.

After crossing the cluster beam at right angles, the XFEL beam exits the vacuum chamber via a beryllium window. The relative x-ray pulse energy was measured shot-by-shot by a p-intrinsic-n (PIN) photodiode, after the pulse energy was reduced by aluminum sheets of 0.2 mm thickness so that the linear response of the photodiode was assured. The shot-by-shot pulse energy fluctuation was ± 25% (50% FWHM).

2.2. Velocity map imaging spectrometer for high energy electrons

For electron spectroscopy at SACLA, we have adopted the velocity map imaging (VMI) technique [43]. Although the VMI technique is well-known, there are some difficulties to use it for studying matter (clusters) in extreme conditions created by the XFEL pulse. In particular we must anticipate high electron energies, of several hundred eV or more. To achieve high energy detection special precautions must be taken and a customised analysis strategy has been adopted. In this subsection we describe the design of the VMI spectrometer for detecting electrons with energies up to ∼1 keV, whereas the details for the analysis procedure for this specific VMI spectrometer will be given in the subsequent

subsection.

Figure 2 depicts a schematic drawing of the VMI spectrometer. The XFEL beam crosses the supersonic gas jet in the region between the U1 and D1 electrodes. Electrons produced by the XFEL irradiation are extracted towards the lower direction by an electrostatic gradient field produced by five electrodes labelled U3, U2, U1, D1 and D2. The distances between U3–U2, U2–U1, U1–D2 and D1–D2 are 15, 10, 10 and 15 mm, respectively. The diameter of the holes of the U3, U2, U1 and D1 are 20 mm, and that of the D2 electrodes are 22 mm. The thickness of these electrodes is 1 mm each. The hole of the U3 electrode is covered with a mesh to terminate the gradient field. The distance between the reaction point and a position-sensitive detector consisting of a set of micro channel plates (MCPs) followed by a phosphor screen is 112 mm.

In the experiment with Xe, the voltages of –7.2, –27.0, –26.2 and –18.1 kV were applied to the U3, U2, U1 and D1 electrodes, respectively, while the D2 electrode and front side of the MCPs were grounded. With these field conditions the electrons emitted into 4π sr with kinetic energies up to ∼960 eV arrive at the detector. The trajectories of electrons emitted perpendicular to the spectrometer axis with kinetic energies of 100, 400 and 900 eV are shown in figure 2 as an example. In the experiment with Ar, the voltages applied to the electrodes were 1/3 of those described above and the energy limit to detect 4π sr was ∼320 eV, because there are no electrons between 300–1000 eV [26].

Electron detection images on the phosphor screen were recorded using a CCD camera synchronized to the arrival of the FEL pulse in the interaction chamber. A 200-ns electrical gate pulse was applied to the back of the MCPs in order to suppress the influence of dark counts on the detector.The measured two-dimensional (2D) projection allows the three-dimensional (3D) momentum distribution of the ejected electrons to be obtained using the inverse Abel transformation.

The dimensions of the electrodes described above are the same as those of the ion spectrometer described in reference [24]. In the present setting, there are also a drift-tube and a delay-line detector beyond the U3 electrode. Thus, we could switch from the VMI spectrometer to the ion spectrometer without opening the vacuum chamber.

2.3. Detection efficiency compensation

In the present VMI spectrometer, the distance between the source point and the MCPs was shorter than in usual VMI configurations [43, 44, 45], in order to collect electrons with energies up to ∼1 keV.In the usual VMI configurations [43, 44, 45], trajectories of all electrons at the detection point are almost perpendicular to the MCP surface. In the present configuration, on the other hand, angles between electron trajectories and MCP surface (θ), and therefore critically their alignment with the MCP channels, depend on the positions where the electrons are detected, as schematically shown in figure 3(a). Thus, trajectories of some electrons were almost parallel to the slanted capillaries of the MCP, resulting in low detection efficiencies, even though we used a two-stage chevron MCPs stack.

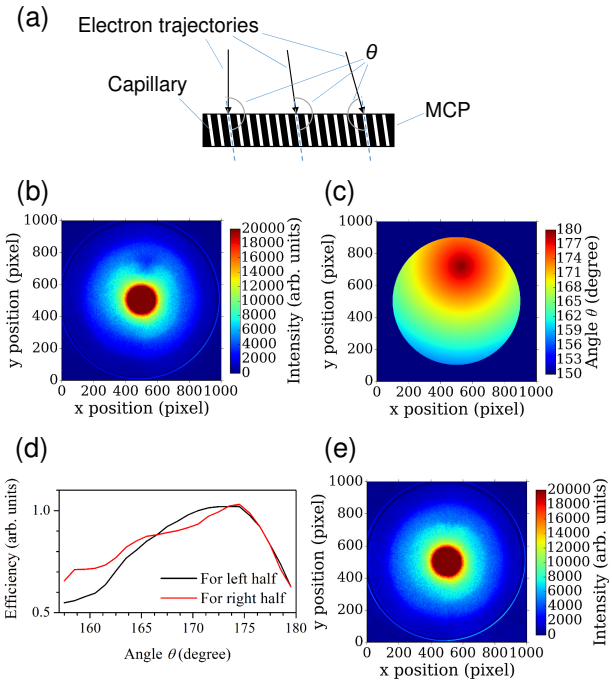

Figure 3. (a) Schematic drawing to explain the geometry of the electron trajectory and the detector. The angle θ is defined as angle between the electron trajectory and the capillaries of the MCP. (b) Raw image of the electron detection from Ar clusters. (c) Relationship between position on the detector and the angle θ. (d) Plots of detection efficiency vs. the angle θ. (e) Compensated image.

Figure 3(b) depicts a raw image of electron detection emitted from Ar clusters irradiated by XFEL. The average cluster size $\langle N \rangle$ is ∼1000. The photon energy is 5 keV and the peak fluence of the XFEL pulses is ∼50 μJ/μm^2. Within the observation energy range ($<$ 320 eV), thermal electrons from nanoplasma and Auger electrons are involved [26]. Since those electrons are emitted isotropically, the detection image should be circularly symmetric. However, the image in figure 3(b) clearly has a low intensity region. We considered that it is due to low detection efficiency. We investigated the relationship between the angle θ and the position on the MCP by using electron trajectory simulations. Figure 3(c) depicts the angle θ as a function of the position on the MCP obtained by the simulations. We confirmed that the position of ∼180 degrees, i.e., the electron trajectory is almost parallel to the MCP capillary, is the same as the position of the low intensity spot in figure 3(b). Assuming that (i) the true intensity distribution is circularly symmetric, and (ii) detection efficiency is a function of the angle, we obtained relative detection efficiencies as a function of angles θ as shown in figure 3(d). We found that the relative detection efficiency varies between 0.5 and 1. Since our CCD camera has different gains for left half and right half, we obtained two efficiency curves for left and right halves. Figure 3(e) depicts the efficiency compensated image from figure 3(a) using figures 3(c) and (d). These corrections were indispensable for extracting the laboratory-frame electron angular distributions, while they were not

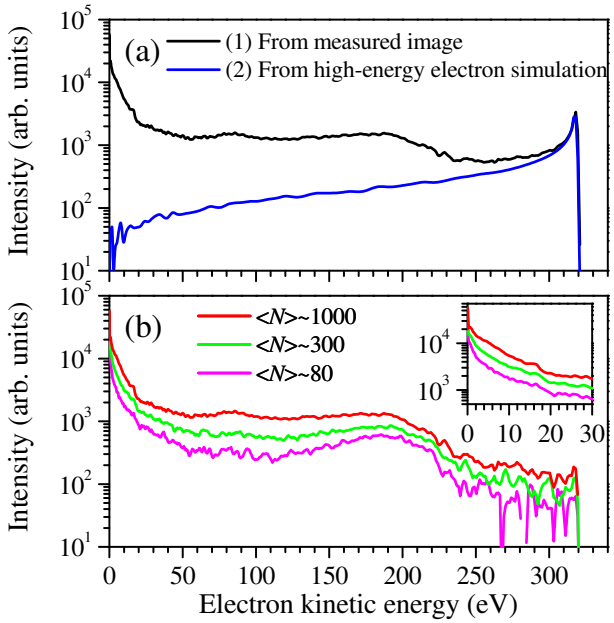

Figure 4. (a) Energy distributions obtained from measured image for Ar cluster ($\langle N\rangle$~1000) and the simulated image assuming the high-energy electron beyond observation region. (b) Electron energy spectra of Ar clusters for different averaged cluster sizes $\langle N\rangle$. Insetted spectra in (b) is expanded ones for low-energy region. The peak fluence of the XFEL pulse is ~50 μJ/μm^2.

significantly affected for the extraction of the electron energy distributions.

2.4. Effects of high-energy electrons beyond the observation range

Even if the energies of electrons are higher than the range of the observation, portions of the electrons, e.g., electrons emitted along the spectrometer axis, arrive at the MCPs and contribute to the detection image. We investigated how such high-energy electrons influence to the electron spectrum.

Figure 4(a) depicts energy distributions obtained after the inverse Abel transformation. The curve (1) is the result of the inversion of the image in figure 3(e). A peak at the high energy edge is an artifact created by high-energy electrons whose energy is beyond the range of observation. In order to estimate the contribution from the high-energy electrons to the spectra, we simulated the image detected by the VMI spectrometer and obtained superficial energy distribution after the inverse Abel transformation. The curve (2) is the superficial energy distribution obtained as a result of the inversion. The detailed procedure to obtain the universal curve (2) is the following. In the first step, we employed a theoretical electron energy distribution reported in [26] for high-energy electrons beyond the range of observation, simulated the image detected by the VMI spectrometer and obtained the superficial energy distribution after the inverse Abel transformation. The curve (2) is in fact the result from this simulation. From a series of simulations varying the energy distributions beyond the

range of observation, we found that the shape of the superficial energy distribution does not depend significantly upon the electron energy distribution beyond the range of observation and thus is well approximated by the curve (2). Also using a full range of theoretical electron spectrum in [26], we found that the energy distribution within the range of observation is well reproduced when the superficial energy distribution given by the curve (2) is subtracted after normalization at the artificial peak. In this way we could subtract contributions from the high-energy electrons beyond the observation range, which provide the artificial structure, without knowing the entire electron energy distributions beyond the range of observation. Electron energy spectra shown in the following are obtained after subtracting contributions from the high-energy electrons beyond the range of observation.

3. Results and discussion

3.1. Electron spectra of Ar clusters irradiated by XFEL

Electron energy spectra of Ar clusters were reported in [26]. Electron energy spectra of Ar clusters depicted in Figure 4(b) are slightly different from the ones reported previously [26] due to a slightly improved analysis. The averaged cluster sizes $\langle N \rangle$ are $\sim$80, $\sim$300 and $\sim$1000. The photon energy is 5 keV and the peak fluence of the XFEL pulse is $\sim$50 μJ/μm^2. In the spectrum for $\langle N \rangle \sim 80$, we can identify the LMM Auger electrons that are emitted following the KLL Auger emission and form the broad peak in the range 150–250 eV. The intensity of continuum electron emission with kinetic energy below 150 eV increases with the increase in the cluster size. When the intense XFEL pulse irradiates the cluster, atoms in the cluster are ionized by photoionization and sequential Auger decay. The cluster gets more charges with the increase in the number of ionized atoms. As a result, the LMM Auger electrons are decelerated by the Coulomb attractive force from the highly-charged cluster ion. The decelerated electrons are eventually trapped by the cluster ion. The LMM Auger electrons and the secondary electrons produced by the low-energy electron impact will also be trapped. As a result, one can expect that a nanoplasma is formed. In the electron spectra, we found thermal electrons that form the peak at zero energy. This thermal electron emission is enhanced with the increase in the cluster size. Inset in the figure 4(b) is a detail of the low energy region. With increasing $\langle N \rangle$, the slope of the thermal emission peaks becomes less steep which indicates that the temperature of the nanoplasma increases with increasing $\langle N \rangle$. We extract a temperature of $\sim$5 eV from the spectrum for Ar_{1000} by fitting an exponential decay function over the electron energy range 0.5–20 eV. With the help of theoretical calculations [26], we could identify that the observed thermal emission is evidence of nanoplasma formation, that the nanoplasma is formed efficiently within the clusters by trapping low-energy electrons, mostly secondary electrons, and that it is formed already during the x-ray pulse of 10 fs duration although the subsequent thermal electron emission lasts long after the pulse is finished.

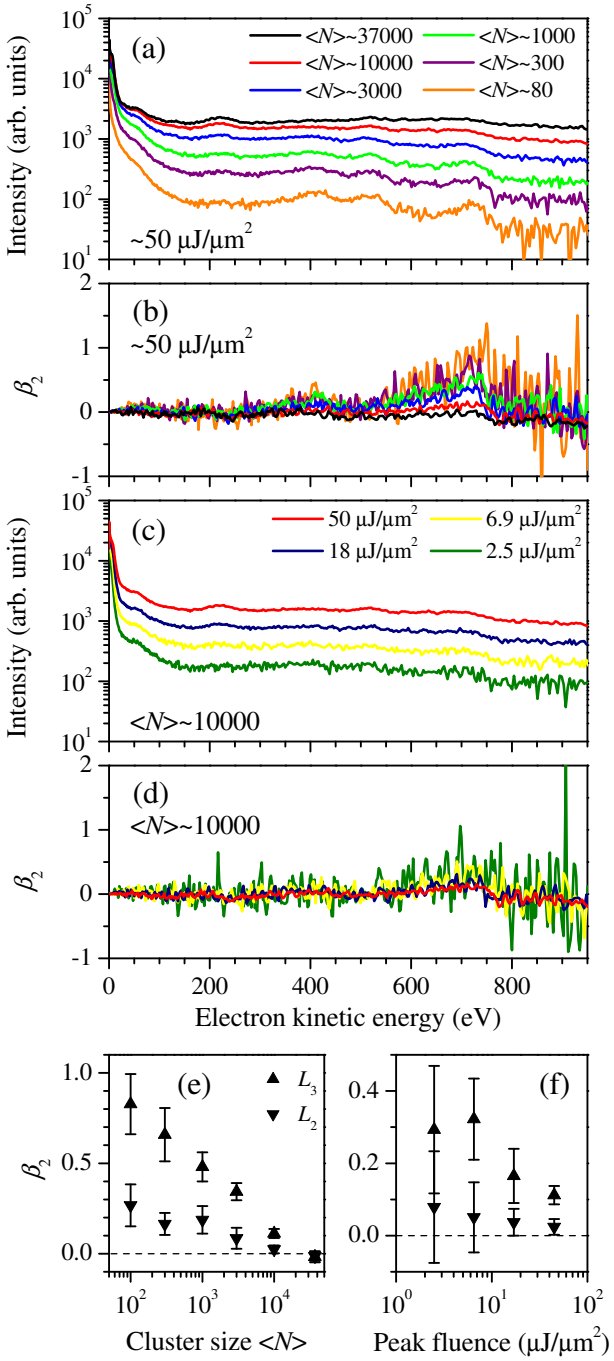

Figure 5. Results of Xe clusters. (a) Electron energy spectra for different averaged cluster sizes $\langle N \rangle$. The peak fluence of the XFEL pulse is $\sim$50 μJ/μm^2. (b) Asymmetry parameter β_2 corresponds to (a). (c) Electron energy spectra for Xe_{10000} at different peak fluences. (d) β_2 corresponds to (c). (e) Cluster size dependence of β_2 averaged within L_2 and L_3 photoelectron peaks. (f) Peak fluence dependence of β_2 averaged within L_2 and L_3 photoelectron peaks.

3.2. Electron spectra of Xe clusters irradiated by XFEL

Figure 5(a) depicts the electron energy spectra from Xe clusters of the different averaged cluster sizes $\langle N \rangle$ at the peak fluence of $\sim$50 μJ/μm^2, The photon energy is 5.5 keV. Since

Xe L_2 and L_3 ionization thresholds are ∼5.1 keV and ∼4.8 keV, respectively, photolines from atomic Xe are located at ∼400 eV and ∼700 eV for the L_2 and L_3, respectively. In the spectrum for $\langle N \rangle$∼80, there are peaks around 400 and 700 eV which correspond to L_2 and L_3 photoemissions, respectively. The peak around 500 eV corresponds to MNN Auger electrons. With increasing $\langle N \rangle$, the valley between the peaks becomes a plateau. These trends are again interpreted as deceleration of photo- and Auger-electrons by the positive electrostatic potential of charged clusters. Kinetic energies of both the $L1$ photoelectron and NOO Auger electron from atomic Xe are ∼50 eV. Contributions of those electrons are not visible because these are overlapped with the strong peak at zero energy from thermal emission from the nanoplasma.

Figure 5(b) depicts the asymmetry parameter β_2 corresponding to figure 5(a). The values of β_2 are close to zero except around the photoelectron region. Generally speaking, photoemissions can have angular dependence with respect to the polarization direction of the incident photons, whereas Auger electrons emit isotropically which corresponds to $\beta_2 = 0$. The thermal emission from the nanoplasma is caused long after the XFEL pulses interaction with the clusters. Thus, the thermal emission from nanoplasma is expected to be also symmetric.

The average of β_2 values within the photoelectron energy region are plotted in figure 5(e). The error bars are estimated from standard deviation of β_2 values within the energy region. The β_2 values for both L_2 and L_3 photoemissions decrease with increasing $\langle N \rangle$. It indicates that photoelectrons are scattered by the atoms in the clusters.

Figure 5(c) depicts the electron energy spectra from Xe clusters with $\langle N \rangle$∼10000 at different peak fluences. Aluminum attenuators with thicknesses of 25, 50 and 75 μm were used to reduce the peak fluence (see figure 1). The shape of the spectra in figure 5(c) does not significantly change with changing peak fluence, except for a false peak at ∼220 eV (see below). Notably the strong peak at zero kinetic energy is observed even in the case of the XFEL peak fluence is 2.5 μJ/μm^2, which corresponds to 2.8×10^9 photons/μm^2. From the photoionization cross section of neutral Xe at 5.5 keV, we estimate that ∼5% of atoms in the clusters are ionized in that case. It indicates the nanoplasma is efficiently produced in the case of Xe clusters due to Auger cascades.

Figure 5(d) depicts the asymmetry parameter β_2 cooresponding to figure 5(c). The values of β_2 are close to zero, except around the same photoelectron region as in figure 5(b). The average of β_2 values within the photoelectron energy region are plotted in figure 5(f). We found that the asymmetry decreases with an increase in the peak fluence. It indicates that in the case of dense nanoplasma, photoelectrons are efficiently scattered by presence of many electrons and ions in the nanoplasma.

We observed another peak at ∼220 eV in both electron spectra in figures 5(a) and (c). This peak strength depends on the cluster size and peak fluence. The corresponding image position on the detector, however, did not change when applied voltages to the electrodes were changed. Thus we consider that the signals do not come from electrons but from photons, e.g., fluorescence from the clusters and/or fragments that are in the

electronically excited states, populated in the excitation and recombination processes of nanoplasma.

4. Conclusions

We have investigated electron emission from Ar clusters and Xe clusters irradiated by the intense XFEL pulse from SACLA, employing a VMI spectrometer specifically designed for studying wide-range energy electron emission from XFEL-produced nanoplasma of solid state densities and high temperatures. We have described how to reliably extract the electron energy spectra and the asymmetry parameters using this VMI spectrometer. Electron emission from Ar clusters were LMM Auger emission decelerated by the Coulomb field of the highly charged parent cluster and secondary electron emission that appears in the form of thermal emission evidencing nanoplasma formation. These electron emissions were isotropic and thus could be used for calibrating the detection efficiencies in order to extract the angular distribution for electron emission from Xe clusters. Electron emission from Xe clusters consists of decelerated L_2 and L_3 photoemission, decelerated MNN Auger emission and very strong thermal emission evidencing nanoplasma formation. Only L_2 and L_3 photoemission exhibits specific angular distributions that become more and more isotropic with the increase in the cluster size and also with the increase in the FEL fluence. The thermal emission is, on the other hand, always isotropic. We infer that the nanoplasma electron density is close to the solid density and its temperature is in the range of a few to 10 eV, i.e., in the so-called range of warm dense matter. We note that nanoplasma formation by trapping of low-energy electrons, mostly secondary electrons, is of universal occurrence whenever matter is irradiated by tightly focused XFEL pulses, whereas photoelectrons predominantly contribute in the nanoplasma formation by EUVFELs.

Acknowledgments

The experiments were performed at SACLA with the approval of JASRI and the program review committee (No. 2012A8036). The authors are grateful to Z. Jurek, S.-K. Son, B. Ziaja and R. Santra for stimulating discussions. This study was supported by the X-ray Free Electron Laser Utilization Research Project and the X-ray Free Electron Laser Priority Strategy Program of the Ministry of Education, Culture, Sports, Science and Technology of Japan (MEXT), by the Japan Society for the Promotion of Science (JSPS) KAKENHI Grant No. 21244062, No. 23241033, by MEXT KAKENHI Grant No. 22740264, by the Proposal Program of SACLA Experimental Instruments of RIKEN, and by the IMRAM project. P.J. acknowledges support from the Swedish Research Council and the Swedish Foundation for Strategic Research. S.M. acknowledges financial support from JSPS. C.M., E.R., and X.J.L. acknowledge a public grant from the Laboratoire dExcellence Physics Atoms Light Matter (LabEx PALM) overseen by the French National Research Agency (ANR) as part of the Investissements

dAvenir program (reference: ANR-10-LABX-0039) and support from the European COST action CM1204XUV/X-ray light and fast ions for ultrafast chemistry (XLIC). R.F. acknowledges the Swedish Research Council (VR) for financial support. JPM and MS acknowledge Engineering and Physical Sciences Research Council (UK) (EPSRC) grant EP/I032517/1 and the ERC ASTEX project 290467.

References

[1] T. Ishikawa *et al.*, Nat. Photonics **6**, 540 (2012).
[2] P. Emma *et al.*, Nat. Photonics **4**, 641 (2010).
[3] M. M. Seibert *et al.*, Nature (London) **470**, 78 (2011).
[4] N. D. Loh *et al.*, Nature (London) **486**, 513 (2012).
[5] Y. Takahashi *et al.*, Nano Lett. **13**, 6028 (2013).
[6] T. Kimura *et al.*, Nat. Commun. **5**, 3052 (2014).
[7] A. Aquila *et al.*, Struct. Dyn. **2**, 041701 (2015).
[8] H. N. Chapman *et al.*, Nature (London) **470**, 73 (2011).
[9] S. Boutet *et al.*, Science **337**, 362 (2012).
[10] L. Redecke *et al.*, Science **339**, 227 (2013).
[11] T. R. M. Barends *et al*, Acta Cryst. D **69**, 838 (2013).
[12] T. R. M. Barends *et al*, Nature (London) **505**, 244 (2014).
[13] C. Kupitz *et al*, Nature (London) **513**, 261 (2014).
[14] M. Suga *et al*, Nature (London) **517**, 99 (2015).
[15] H. M. Quiney and K. A. Nugent, Nat. Phys. **7**, 142 (2011).
[16] O. Yu. Gorobtsov, U. Lorenz, N. M. Kabachnik, and I. A. Vartanyants, Phys. Rev. E **91**, 062712 (2015).
[17] H. Thomas, *et al.*, Phys. Rev. Lett. **108**, 133401 (2012).
[18] T. Gorkhover *et al.*, Phys. Rev. Lett. **108**, 245005 (2012).
[19] H. Yoneda *et al.*, Nat. Commun. **5**, 5080 (2014).
[20] S. M. Vinko *et al.*, Nat. Commun. **6** 6397 (2015).
[21] H. Yoneda *et al.*, Nature (London) **524**, 446 (2015).
[22] B. Nagler *et al.*, J. Synchrotron Rad. **22**, 520 (2015).
[23] H. Fukuzawa *et al.*, Phys. Rev. Lett. **110**, 173005 (2013).
[24] K. Motomura *et al.*, J. Phys. B: At. Mol. Opt. Phys. **46**, 164024 (2013).
[25] K. Motomura *et al.*, J. Phys. Chem. Lett. **6**, 2944 (2015).
[26] T. Tachibana *et al.*, Sci. Rep. **5**, 10977 (2015).
[27] T. Laarmann *et al.*, Phys. Rev. Lett. **95**, 063402 (2005).
[28] U. Saalmann, Ch. Siedschlag and J. M. Rost, J. Phys. B **39**, R39 (2006).
[29] C. Bostedt *et al.*, Phys. Rev. Lett. **100**, 133401 (2008).
[30] B. Ziaja *et al.*, New J. Phys. **11**, 103012 (2009).
[31] Th. Fennel *et al.*, Rev. Mod. Phys. **82**, 1793 (2010).
[32] C. Bostedt *et al.*, J. Phys. B **43**, 194011 (2010).
[33] C. Bostedt *et al.*, New J. Phys. B **12**, 083004 (2010).
[34] M. Arbeiter and Th. Fennel, New J. Phys. **13**, 053022 (2011).
[35] S. Yase *et al.*, Phys. Rev. A **88**, 043203 (2013).
[36] M. Yabashi *et al.*, J. Phys. B: At. Mol. Opt. Phys. **46**, 164001 (2013).
[37] K. Tono *et al.*, New J. Phys. **15**, 083035 (2013).
[38] H. Yumoto *et al.*, Nature Photon. **7**, 43 (2013).
[39] K. Nagaya *et al.*, J. Electron Spectrosc. Relat. Phenom. **181**, 125 (2010).
[40] O. Hagena and W. Obert, J. Chem. Phys. **56**, 1793 (1972).
[41] R. Karnbach *et al.*, Rev. Sci. Instrum. **64**, 2838 (1993).

[42] U. Buck and R. Krohne, J. Chem. Phys. **105**, 5408 (1996).
[43] A. T. J. B. Eppink and D. H. Parker, Rev. Sci. Instrum. **68**, 3477 (1997).
[44] A. Rouzee *et al.*, Phys. Rev. A **83**, 031401(R) (2011).
[45] S. Mondal *et al.*, J. Phys. B: At. Mol. Opt. Phys. **46**, 205601 (2013).